Homogenization of a Reaction Diffusion Equation can Explain Influenza A Virus Load Data

Arwa Abdulla Baabdulla[a,*], Hesung Now[b], Ju An Park[c], Woo-Jong Kim[b], Sungjune Jung[c,d], Joo-Yeon Yoo[b], Thomas Hillen[a]

[a] *Department of Mathematical and Statistical Sciences, University of Alberta, Edmonton, Alberta, Canada*
[b] *Department of Life Sciences, Pohang University of Science and Technology, Pohang, Republic of Korea*
[c] *Department of Creative IT Engineering, Pohang University of Science and Technology, Pohang, Republic of Korea*
[d] *School of Interdisciplinary Bioscience and Bioengineering, Pohang University of Science and Technology, Pohang, Republic of Korea*

Abstract

We study the influence of spatial heterogeneity on the antiviral activity of mouse embryonic fibroblasts (MEF) infected with influenza A. MEF of type $Ube1L^{-/-}$ are composed of two distinct sub-populations, the strong type that sustains a strong viral infection and the weak type, sustaining a weak viral load. We present new data on the virus load infection of $Ube1L^{-/-}$, which have been micro-printed in a checker board pattern of different size of the inner squares. Surprisingly, the total viral load at one day after inoculation significantly depends on the sizes of the inner squares. We explain this observation by using a reaction diffusion model and we show that mathematical homogenization can explain the observed inhomogeneities. If the individual patches are large, then the growth rate and the carrying capacity will be the arithmetic means of the patches. For finer and finer patches the average growth rate is still the arithmetic mean, however, the carrying capacity uses the harmonic mean. While fitting the PDE to the experimental data, we also predict that a discrepancy in virus load would be unobservable after only half a day, and that the carrying capacity would be reached within 2.5-4.5 days.

*CAB 632, University of Alberta, Edmonton, Alberta, T6G 2G1

Email addresses: baabdull@ualberta.ca (Arwa Abdulla Baabdulla), thillen@ualberta.ca (Thomas Hillen)

Keywords: Virus load, spatial viral distribution, Homogenization method, Fisher-KPP equation, Arithmetic mean, Harmonic mean

1. Introduction

In experiments of mouse embryonic fibroblasts (MEF), we infected MEF of type $Ube1L^{-/-}$ with influenza A virus to observe their susceptibility and resistance to viral infection. The fibroblast population is bimodal, consisting of cells that sustain a strong or weak virus infection, respectively (Now and Yoo, 2016). In typical cell experiments, these cells are mixed, forming a homogeneous population. The importance and correlation between the virus infection and population with heterotypic patterns has been studied in (Snijder et al., 2009). However, the effects of spatial complexity between heterogeneous population has not been explored yet. Therefore, it is of interest to understand whether the viral susceptibility changes when the spatial distribution of the sub-populations becomes heterogeneous.

To analyse this question, (Park et al., 2017) employed a brand new cell-printing method, which allowed to print cell cultures in a checker board pattern, where the two cell populations are separated into little squares (see Figure 1 a). The size of the inner squares can be adjusted from almost complete separation (large squares), to finely mixed (small squares), to fully mixed. In Park et al. (Park et al., 2017), the experimental plates had 50% of A549 human alveolar lung epithelial cells, and 50% of HeLa cervical cancer cells. These two cell lines are known to possess relatively "strong" and "weak" infectivity to influenza A, respectively (Li et al., 2009; De Vries et al., 2011). To their surprise, the total virus load did *" not arise as a simple arithmetic summation of the individual cellular activities"*. Here we repeat the experiments with mouse embryonic fibroblasts (MEF) of type $Ube1L^{-/-}$ using 50% "weak infectivity" sub-type and and 50% "strong infectivity" sub-type. Similar to the experiments of (Park et al., 2017) we also find that the total virus load after one day of inoculation depends on the spatial arrangement of the cells. The finely mixed and fully mixed plates had a much reduced total viral load as compared to the large scale patterns (see data in Figure 1 b), suggesting a strong dependence of the total viral load on the spatial arrangement.

In this paper we use mathematical modelling to explain the spatial dependence of the virus load data. Mathematical modelling of virus load is

an active field of research (see Smith and Perelson (2011); Beauchemin and Handel (2011); Gallagher et al. (2018); Smith (2018)). While most of these models are based on ordinary differential equations, a few approaches use spatial modelling (Gallagher et al. (2018); Wodarz et al. (2012); de Rioja et al. (2016)). Here we base our model on a Fisher-KPP reaction-diffusion model (Murray, 2007) and we use homogenization methods and numerical methods to analyze the model. To say it upfront, while going from coarse to fine mixture, we observe a transition from an arithmetic mean of two steady state virus load levels to a harmonic mean to these values. As the harmonic mean is always smaller than the arithmetic mean, it explains the observed reduction in virus load for the finer mixed experiments. As we calibrate the model to our experimental data we find that the model cannot only explain the observed virus load data, it can also predict values that were not measured in the experiments. For example, we find from the modelling that the homogenization effect would not be visible within error tolerances after 1/2 day, which was confirmed in personal conversations later. We also find that the virus load population has not reached steady state after one day, and multiple day experiments would be desirable. However, we understand that the cells suffer from the virus infection and after one day many of them start dying. Moreover, we found the spatial viral load distribution across the periodic domain by solving the mathematical model numerically.

Our analysis shows a simple but relevant example of the effect of spatial heterogeneity on cell responses to virus infection. It shows that measurements done on cell populations in isolation cannot simply be carried over to a heterogeneous mixture of cells. The spatial arrangement seems to be important.

1.1. Outline

The paper is organized as follows: In the next section (Section 2) we explain the experimental set up and the data collection. In Section 3 we introduce the mathematical model. We chose a very classical Fisher-KPP reaction-diffusion equation (Murray, 2007), which is quite sufficient for our purpose. We then perform the spatial homogenization as it is relevant for our problem. From this analysis the dichotomy between arithmetic and harmonic means arises. In Section 4 we fit our model to our virus-load data using a log-likelihood method, thereby explaining the observed virus load dependence on the spatial arrangement. In Section 5 we present numerical solutions of the corresponding model, which show the spatial distribution of the viral

infection across the checker board pattern. We close with a discussion in section 6.

2. Influenza A Infection Experiments

We consider mouse embryonic fibroblast (MEF) of $Ube1L^{-/-}$, where $Ube1L$ stands for a ubiquitin like modifier activating enzyme for ISGylation protein that conjugates an Interferon (IFN) stimulated gene 15 (ISG15) to target proteins. The $Ube1L^{-/-}$ are null mutations of $Ueb1L$, where the $Ueb1L$ production is deactivated. Studying these cells, we found that $Ube1L^{-/-}$ populations are bimodal, with two sub-populations of differential antiviral activity (Now and Yoo, 2016). $Ube1L^{-/-}(S)$ and $Ube1L^{-/-}(W)$ designates those subpopulations with *strong* and *weak* infectivity, respectively.

To study the influence of the spatial distribution patterns on the virus load of the population as a whole, we printed $Ube1L^{-/-}(S)$ and $Ube1L^{-/-}(W)$ cells in a regular checker board pattern by using the inkjet bio-printing system (Park et al., 2017). While fixing the size of the checker board square to $30 \times 30\ mm^2$, the size of the inner squares has been variable using side lengths of 1.5 mm, 3 mm, 5 mm, and fully mixed, (see Figure 1a). Thus, the geometric separation of $Ube1L^{-/-}(S)$ and $Ube1L^{-/-}(W)$ cells is increased as the size of the inner squares is increased. The mixed case of 50/50 of $Ube1L^{-/-}(S)$ and $Ube1L^{-/-}(W)$ cells is used as a control. In each of these experiments, the cells on the checker board and the mixed plate were infected with Influenza A virus and incubated for 24 hours. The infected cells were harvested and the total amount of intracellular viral genome was measured using the real time quantitative PCR method (Figure 1b). Two independent experiments with triplicate data sets were used (see data in Appendix A).

The method of Livak (Delta Delta CT) has been used to compute the relative quantification (gene expression)

$$RQ = 2^{-(\Delta\Delta CT)},$$

where CT represents the cycle number where the fluorescence that is generated by the PCR is distinguishable from the background noise cycle threshold (CT) of our sample. We measure ΔCT by the following formula

$$\Delta CT = CT(\text{target gene}) - CT(\text{reference gene}).$$

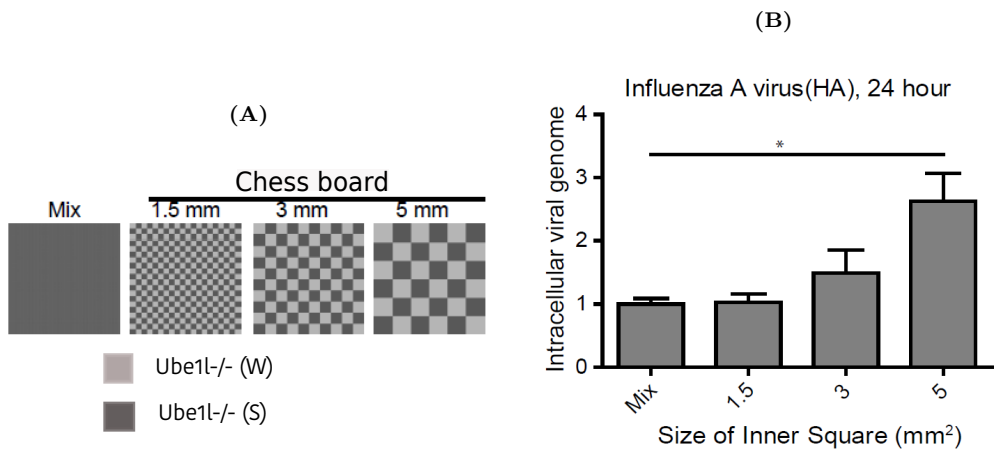

Figure 1: **(A):** Design of cell-printing pattern, **(B):** Relative amount of viral genome.

Here, our target gene is influenza A hemagglutinin (HA) gene and the reference gene is the mouse glyceraldehyde 3-phosphate dehydrogenase (mGAPDH) gene. Thus, we can compute $\Delta\Delta CT$ as the following

$$\Delta\Delta CT = \Delta CT(\text{experimental sample}) - \Delta CT(\text{control sample}),$$

where the control sample is the first experiment with inner square side length of 1.5 mm. The full raw data set is shown in Appendix A and a summary is given in Figure 1 b).

Looking at the virus load data in Figure 1 b, we can see clearly a mismatch in the viral load depending on the inner square size from mix, to 1.5 mm, to 3 mm and to 5 mm. However, each experiment has the same ratio and the same mass of $Ube1L^{-/-}$ (W) and (S) cells. Therefore, the antiviral activity of the cell population as whole is not a simple summation of the individual cellular activities. Furthermore, after the 12 hours of infection, there was no significant mismatch in the viral load between the different inner square sizes, and was only recorded after 24 hours and thereafter.

3. A Mathematical Model

Reaction diffusion equations (RDE) are a powerful tool whenever the spatial spread of a population is of importance. One of the simplest examples

of a RDE equation is the Fisher-KPP equation

$$\frac{\partial}{\partial t}v(x,t) = D\frac{\partial^2}{\partial x^2}v(x,t) + \mu(x)v(x,t)\left(1 - \frac{v(x,t)}{K(x)}\right), \tag{1}$$

where $v(x,t)$ is the viral density at time t and location x, D is the diffusion coefficient, describing the spatial spread of invective virus, μ is the population growth rate of the virus, and K is the population carrying capacity. Since the model is used to describe the spatially varying checker board patterns, we assume that the growth rate $\mu(x)$ and the virus carrying capacity $K(x)$ are spatially dependent. We assume that the transport of virus from cell to cell is the same for all cell types, hence we assume D is not spatially dependent and it is constant. The model can be considered for the case of $D(x)$ as well (see Shigesada et al. (1986, 2015); Maciel and Lutscher (2013)), but the model with constant D is sufficient to explain our data. Moreover, we have no biological indication to assume that the diffusivities should be different, hence we assume they are the same.

Fisher proposed equation (1) in his paper *"The wave of advance of advantageous genes"* in 1937 (Fisher, 1937). He studied the diffusion of species in one dimension and its traveling wave solutions with considering the reaction term being logistic. In the same year, Kolmogorov, Petrovsky, and Piskunov studied the reaction diffusion equation in two dimensions and with more general monostable reaction term (Kolmogorov et al., 1937).

The parameters of the Fisher-KPP equation (1) will be estimated based on the data from the experiments which we presented in the previous Section 2.

3.1. Homogenized Fisher KPP Model

The experimental set up as described above is a paradigm for a homogenization problem. A microscopic scale (inner squares) is varied on a finer and finer scale, until in the limit, a homogeneous mixture arises. We are in the fortunate position, that not only the separated and fully mixed states are measured, but also several intermediate values for intermediate mixture types. While homogenization is a well known scaling method in physical applications (Pavliotis and Stuart, 2008; Holmes, 2012), it has only recenlty been used for ecological problems in (Garlick et al., 2011; Maciel and Lutscher, 2015; Yurk, 2018; Yurk and Cobbold, 2018). To our knowledge, this method has never been used in the microbiological context considered here.

Due to the symmetry of the problem, we present the argument in a one-dimensional setting. The scaling method applies to higher dimensions as well, but the one-dimensional setting is sufficient for our purpose. To model the specific checker board pattern, we divide the real line into small intervals of equal length, which separates weak and strong infectivity populations (see Figure 2). On this periodic domain we consider the spatial dependent Fischer-KPP equation (1), where the virus growth rate $\mu(x)$ and the virus load carrying capacity $K(x)$ vary between cell types, i.e.

$$K(x) = \begin{cases} K_W, & x \in \text{ patch of type weak} \\ K_S, & x \in \text{ patch of type strong} \end{cases} \tag{2}$$

$$\mu(x) = \begin{cases} \mu_W, & x \in \text{ patch of type weak} \\ \mu_S, & x \in \text{ patch of type strong.} \end{cases}$$

We use W to indicate the $Ube1L$ sub-population of weak infectivity and S for strong infectivity. For the general analysis we simply consider periodic functions $K(x)$, $\mu(x)$.

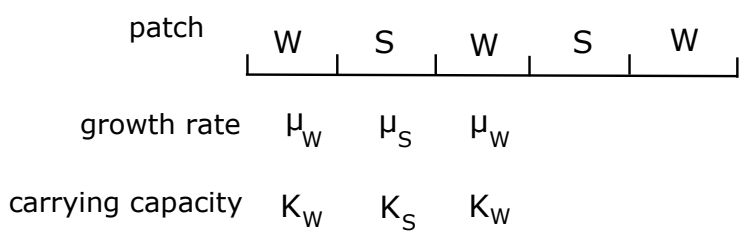

Figure 2: Sketch of a periodic patchy environment of two cell types.

We like to distinguish two relevant spatial scales, the scale of the individual patches y, represented by the inner squares and the global scale of the whole experiment x, represented by the chess board printing. Also, we assume that there is a small parameter $\epsilon > 0$ such

$$y = \frac{x}{\epsilon},$$

where ϵ represents the ratio between the local and global scales. In the experiment,

$$\epsilon = \frac{\text{the size of inner square}}{\text{the size of the chess board}}.$$

Thus, we can compute the ϵ for the 5 mm, 3 mm, and 1.5 mm inner squares as $\epsilon = 1/6, 0.1, 0.05$, respectively.

We use standard assumptions in homogenization (see e.g. (Pavliotis and Stuart, 2008)) and assume that the growth rate $\mu(y)$ and the carrying capacity $K(y)$ change only on the small scale y and they do not vary on the large scale x. The virus load depends on both scales, $v(x, y, t)$ and the partial derivatives change as

$$\frac{d}{dx}v(x, y(x), t) = \frac{\partial}{\partial x}v(x, y, t) + \frac{1}{\varepsilon}\frac{\partial}{\partial y}v(x, y, t)$$

If we introduce this assumption into (1) we get the multiscale reaction-diffusion equation

$$\begin{aligned}\frac{\partial}{\partial t}v(x, y, t) = \frac{D}{\varepsilon^2}\frac{\partial^2}{\partial y^2}v(x, y, t) + \frac{2D}{\varepsilon}\frac{\partial^2}{\partial x \partial y}v(x, y, t) + D\frac{\partial^2}{\partial x^2}v(x, y, t) \\ +\mu(y)v(x, y, t)\left(1 - \frac{v(x, y, t)}{K(y)}\right). \end{aligned} \tag{3}$$

To analyze this equation we use a perturbation expansion in the small parameter ε:

$$v(x, y, t) = v_0(x, y, t) + \varepsilon v_1(x, y, t) + \varepsilon^2 v_2(x, y, t) + \cdots, \tag{4}$$

where all functions $v_j(x, y, t), j = 0, 1, 2, \ldots$ are assumed to be periodic in y of period 1.

We substitute this expansion (4) into (3) and collect terms of equal order in ε. The leading order term is of order ε^{-2}:

- ε^{-2} : We obtain $0 = D\frac{\partial^2}{\partial y^2}v_0(x, y, t)$, which leads to a general form

  $$v_0(x, y, t) = c_1(x, t)y + c_2(x, t)$$

  Since $v_0(x, y, t)$ is periodic in y, the first term $c_1 = 0$ and we find that v_0 does not depend on y. We write $v_0(x, t)$ instead of using $c_2(x, t)$.

- ε^{-1} : In this case we find

  $$0 = D\frac{\partial^2}{\partial y^2}v_1(x, y, t) + 2D\frac{\partial^2}{\partial x \partial y}v_0(x, t).$$

  Since v_0 does not depend on y, the second term is zero. Hence the first term is zero as well. Again arguing with periodicity, we find that also v_1 is independent of y and we write $v_1(x, t)$.

- ε^0 : Here we find

$$\frac{\partial}{\partial t}v_0(x,t) = D\frac{\partial^2}{\partial y^2}v_2(x,y,t) + 2D\frac{\partial^2}{\partial x \partial y}v_1(x,t) + D\frac{\partial^2}{\partial x^2}v_0(x,t) + \mu(y)v_0(x,t)\left(1 - \frac{v_0(x,t)}{K(y)}\right). \tag{5}$$

  Instead of solving this equation for v_2 we simply integrate over one period $y \in [0,1]$: Since v_0 and v_1 do not depend on y, several terms simplify. We find the homogenized equation:

$$\frac{\partial}{\partial t}v_0(x,t) = D\frac{\partial^2}{\partial x^2}v_0(x,t) + \int_0^1 \mu(y)dy\ v_0(x,t) - \int_0^1 \frac{\mu(y)}{K(y)}dy\ v_0^2(x,t). \tag{6}$$

To understand (6) we introduce the *arithmetic mean* and the *harmonic mean* as

$$\langle \mu \rangle_a = \int_0^1 \mu(y)dy, \qquad \langle K \rangle_h = \left(\int_0^1 \frac{1}{K(y)}dy\right)^{-1}$$

and we consider three cases:

Case 1: Consider $K(y) = K$ constant. Then (6) becomes a standard Fisher-KPP equation

$$\frac{\partial}{\partial t}v_0 = D\frac{\partial^2}{\partial x^2}v_0 + \langle \mu \rangle_a v_0\left(1 - \frac{v_0}{K}\right), \tag{7}$$

where the homogenized growth rate $\langle \mu \rangle_a = \frac{1}{2}(\mu_S + \mu_W)$ is the arithmetic mean of $\mu(y)$.

Case 2: Consider $\mu(y) = \mu$ constant. In this case (6) becomes

$$\frac{\partial}{\partial t}v_0 = D\frac{\partial^2}{\partial x^2}v_0 + \mu v_0\left(1 - \frac{v_0}{\langle K \rangle_h}\right), \tag{8}$$

where the carrying capacity arises as harmonic mean of $K(y)$:

$$\langle K \rangle_h = \frac{1}{\frac{1}{2}\left(\frac{1}{K_S} + \frac{1}{K_W}\right)}.$$

Case 3: We can also write the general homogenized equation (6) as a Fisher-KPP equation, however, with less intuitive average terms as

$$\frac{\partial}{\partial t}v_0 = D\frac{\partial^2}{\partial x^2}v_0 + \langle\mu\rangle_a v_0\left(1 - \frac{v_0}{\langle\mu\rangle_a\left(\langle\frac{\mu}{K}\rangle_a\right)^{-1}}\right). \tag{9}$$

Here the effective growth rate and effective carrying capacity are

$$\tilde{\mu} = \langle\mu\rangle_a, \qquad \tilde{K} = \frac{\langle\mu\rangle_a}{\langle\frac{\mu}{K}\rangle_a}. \tag{10}$$

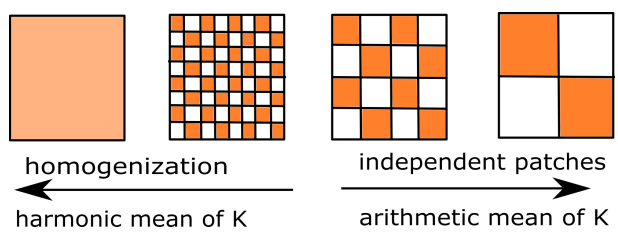

Figure 3: Sketch of a period patchy environment and the homogenization limit.

As illustrated in Figure 3, the fine printing of the virus hosts in patches of different sizes leads to different averaging. If the individual patches are large, then they can be considered as almost independent, and the growth rate and the carrying capacity will be the arithmetic means $\langle\mu\rangle_a, \langle K\rangle_a$ of the patches. On the other hand, for finer and finer patches we have shown that the average growth rate is still the arithmetic mean $\langle\mu\rangle_a$, however, the carrying capacity uses the harmonic mean. For example in Case 2 above it is $\langle K\rangle_h$ and it is known that

$$\frac{1}{\frac{1}{2}\left(\frac{1}{K_S} + \frac{1}{K_W}\right)} = \langle K\rangle_h \leq \langle K\rangle_a = \frac{1}{2}(K_S + K_W), \tag{11}$$

where equality is satisfied when $K_S = K_W$. Hence a reduction of the overall carrying capacity for finer patches is a direct consequence of the averaging procedure.

4. Application to the Fibroblast Experiments

Case 1, where $K(y)$ =const., cannot describe the observed data, since the averaging of the growth rate does not change from coarse to fine experiments.

However, Cases 2 and 3 can. Since Case 2 is nested in Case 3, and since Case 2 is sufficient to explain the observed phenomenon, we focus our analysis on Case 2, where the virus growth rate μ is (almost) constant between the two cell types, while the carrying capacities are significantly different:

$$\mu = \mu_S = \mu_W, \qquad \text{and} \qquad \langle K \rangle_h = \frac{1}{\frac{1}{2}\left(\frac{1}{K_S} + \frac{1}{K_W}\right)}.$$

4.1. Calibration I: Naive Approach

Based on the above calculations it is straight forward to simply compare the arithmetic means and harmonic means with the available data. We will find that some of the data can be explained, but not all, which will motivate us to make use of the full PDE formulation in a subsequent section.

In Table 2 we show the virus load data that correspond to the data shown in Figure 1 b. Notice that the data in Figure 1 b are normalized to the mixed case, while the data in Table 1 are the original data.

Inner Square	**Mix**	**1.5 mm**	**3 mm**	**5mm**
Mean	1.2957	1.3305	1.9304	3.3996
Stand. Dev.	0.2002	0.2917	0.8111	0.9968
Stand. Error	0.1156	0.1684	0.4683	0.5755
Error Bar	$[1.1801, 1.4113]$	$[1.1621, 1.4989]$	$[1.4621, 2.3986]$	$[2.8241, 3.9751]$

Table 1: Virus load data, standard deviation and error bars.

We assume for now that the 5 mm plate corresponds to the separated case, i.e. $\langle K \rangle_a = 3.3996$, while the mixed case corresponds to the harmonic mean $\langle K \rangle_h = 1.2957$. To find K_S, K_W we then simply solve the two equations for the means (11) to find

$$K_W = 0.7252, \quad \text{and} \quad K_S = 6.0740.$$

To investigate the agreement with the intermediate cases of 1.5 mm and 3 mm, we use the above parameter values and solve the full PDE (1). For this we also need the diffusion constant D and the virus growth rate μ. We can evaluate the diffusion coefficient by applying the Stokes-Einstein equation for the diffusion coefficient D of a spherical particle of radius r in a fluid of

dynamic viscosity η at absolute temperature T (Murray and Jackson, 1992)

$$D = \frac{k_B T}{6\pi\eta r} = 0.5 \text{ mm}^2 \text{ per day},$$

where k_B is Boltzmann's constant, $r = 50\,nm$ is a typical virus size, and $\eta = 0.00078\ pa.\,s$ is the viscosity of DMEM (10 % FBS) medium at $T = 37^oC$ (Bacabac et al., 2005).

From the data, we found a range of values of the growth rate for the virus in weak and strong infectivity cells. While $\mu_W \in [0.1155, 0.3547]$, we found $\mu_S \in [0.1155, 0.4722]$. Therefore, we choose the intermediate value $\langle\mu\rangle_a = 0.23$ per hour.

We use a Forward-Time-Central-Space (FTCS) (Smith, 1985) scheme to solve the equation (1) with step size $\Delta x = 0.1$ and $\Delta t = 0.008$. More detail on the numerical method and on typical solutions is given in Section 5. For the naive case here we present the resulting virus load values in Table 2.

Day	**0.5**	**1**	**1.5**	**2**	**2.5**	**3**
Mix	0.73718	1.2365	1.2918	1.2955	1.2957	1.2957
1.5mm	0.75627	1.380	1.4845	1.4952	1.4962	1.4963
3mm	0.79282	1.7304	2.0011	2.0406	2.0457	2.0463
5mm	0.83085	2.1431	2.5917	2.6525	2.6595	2.6603

Table 2: Simulated virus load data up to three days.

We observe, see red curve in Figure 5, that after one day the mix, 1.5 mm, and 3 mm plate values are reproduced within error bars, while the 5 mm plate value is below the error bar of the 5mm measurements.

4.2. Calibration II: PDE Approach

The above mismatch for the 5 mm plate is related to the fact that the 5 mm squares are still relatively mixed, and they might not correspond to the a fully separated state. Hence, numerically, we test this hypothesis by including a hypothetical 15 mm case, where the cell types are separated into one compartment for weak infectivity and one compartment for strong infectivity responding cells. As the corresponding virus load has not been measured (due to technical limitations of the bio-printing method), we use a

least-squares approach to estimate the missing value. We minimize

$$E = \sum_{i=1}^{4} (M_i \text{ value} - PDE_i \text{ value})^2, \tag{12}$$

where i= 1,2,3,4 represent the inner squares sizes: mix, 1.5 mm, 3 mm, and 5 mm respectively. M_i denotes the measurement value and PDE_i the integral of the solution curve of the PDE. We find that, when $K_{15mm} \in [6.3, 19.1]$, with values of $K_W \in [0.6592, 0.6851]$ and $K_S \in [11.915, 37.541]$ are within the standard errors of each inner square size. In addition, the minimum error $E = 0.0974$ is obtained when

$$K_{15} = 9.6000, \quad \text{with} \quad K_W = 0.6713 \quad \text{and} \quad K_S = 18.529$$

(see Figure 4) .

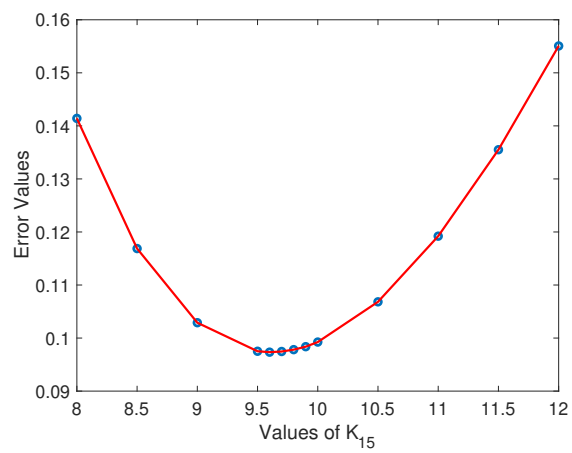

Figure 4: The values of K_{15} and Error values at 24 hours.

In Table 3 and Figure 5 we compare the measured values to the optimized PDE results and also record the error and relative error when $K_{15} = 9.6000$ at t=24. We see that the model results are very close to the measurement, well within the error bars. A fit of this level of accuracy is quite uncommon for biological data, and we are confident that the optimized PDE model does explain the data well.

Size of Inner Square	Measurement	PDE	Error^2	Relative Error
Mix	1.2957	1.2365	0.0035	4.6 %
1.5mm	1.3305	1.4635	0.0177	10 %
3mm	1.9303	2.1889	0.0669	13.4 %
5mm	3.3996	3.3033	0.0093	2.8 %
Least Square Error			0.0974	

Table 3: Comparison of the measurements with the optimized PDE model.

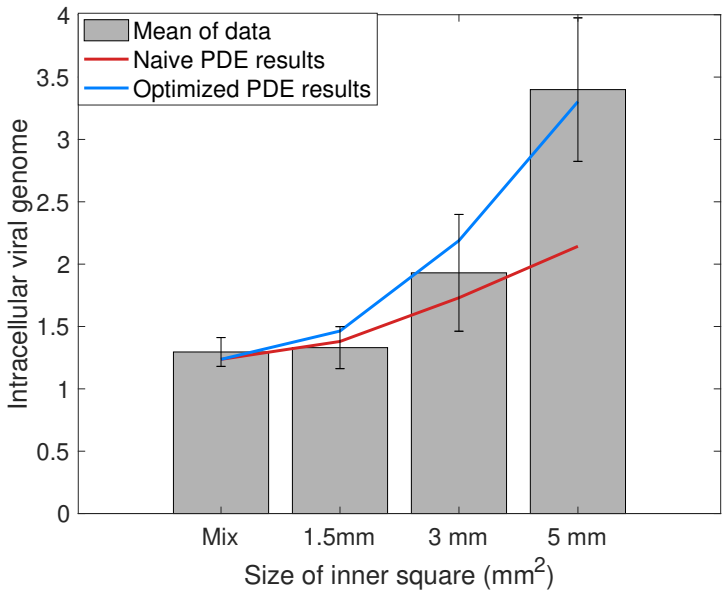

Figure 5: The data with naive PDE results and optimized PDE results

We further use our optimized PDE model to investigate the virus load after 0.5 days as well. For the mix, 1.5mm, 3mm, 5mm, and 15mm we find simulated virus load numbers of 0.7372, 0.7643, 0.8183, 0.8766, and 0.9561, respectively. Although there is a slight increase from mixed to separated, the difference is small and would not be observable in measurements. An observation that is confirmed in our experiments (experimental values not shown).

5. Numerical Analysis of the PDE Model

After having optimized the PDE model with the experimental data, we like to benefit from the availability of this model, and study the spatial viral-load distribution. We will find an interesting artifact in that solutions overshoot at one of the boundaries.

5.1. Mix Plate

Since $\mu_S = \mu_W$, we can solve the homogenized equation (8) for the Case 2 by the Forward-Time-Central-Space (Smith, 1985). As μ and K are constant and the initial condition is non-negative, the solution should converge to the carrying capacity $K_{Mix} = \langle K \rangle_h = 1.2957$, which has been confirmed numerically as shown in Figure 6 (A).

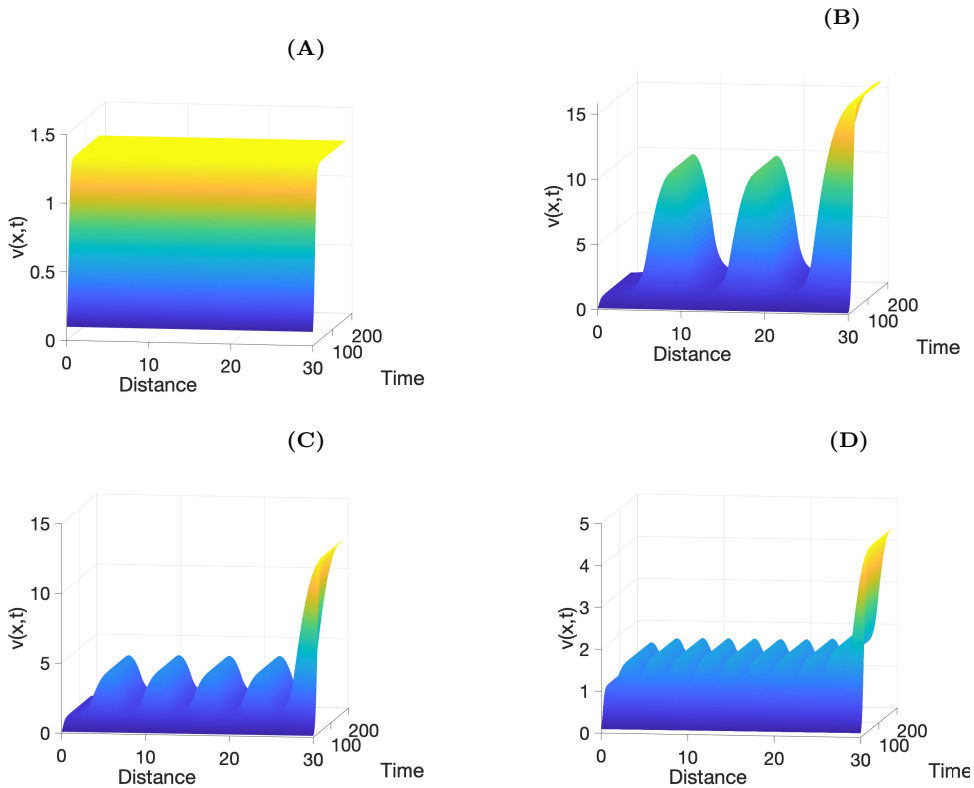

Figure 6: Numerical simulation when $\mu_S = \mu_W = 0.23$ with $v(x,0) = 0.1$, and $v_x(0,t) = v_x(30,t) = 0$ for **(A):** mix plate, **(B):** 5 mm inner square, **(C):** 3 mm inner square, **(D):** 1.5 mm inner square.

5.2. Spatially Printed Plates

For the spatially printed plates, we consider two patches, "strong" which represent strong infectivity cells and "weak" which represent weak infectivity cells. Accordingly, the carrying capacity is spatially constant within a patch but different between patches. While, the diffusion coefficient D and growth rate μ are the same in the two patches. We partition the entire interval into sub-intervals ('patches') (y_{i-1}, y_i), $i \in \mathbb{N}$. Thus, we have

$$\frac{\partial v_i}{\partial t} = D\frac{\partial^2 v_i}{\partial y^2} + \mu_i v_i \left(1 - \frac{v_i}{K_i}\right), \text{ for } y \in (y_{i-1}, y_i).$$

We define transition conditions that link the population densities and population fluxes between adjacent patches as follows.

1. Since the diffusion coefficient does not vary between the patches, the flux is continuous across an interface

$$\partial_y v(y_i^+, t) = \partial_y v(y_i^-, t).$$

   Here, y_i^+ and y_i^- denote right and left sided limits at y_i.
2. The probability of individual at interface y_i moving to the right or left is the same and equal to 0.5 Thus

$$v(y_i^+, t) = v(y_i^-, t),$$

   which ensures continuity of the solution at the interfaces.

The simulations for the mix, 5 mm, 3 mm and 1.5 mm printed plates can be found in Figure 6 (B)-(D).

All the estimated values of the parameters from the experimental data are summarized in Table 4:

Parameter	**Description**	**Value**	**Unit**
D	Diffusion coefficient	0.5000	$\text{mm}^2\text{day}^{-1}$
$\langle\mu\rangle_a$	Arithmetic mean of maximum growth of rate	0.2300	hour^{-1}
K_W	Carrying capacity of weak infectivity cells	0.6713	viral load
K_S	Carrying capacity of strong infectivity cells	18.529	viral load
$\langle K\rangle_a$	Arithmetic mean of carrying capacity	9.6000	viral load
$\langle K\rangle_h$	Harmonic mean of carrying capacity	1.2957	viral load
K_{Mix}	Carrying capacity of mixed printed plate	1.2957	viral load
K_{15mm}	Carrying capacity of 15 mm printed plate	9.6000	viral load

Table 4: Summary of calibrated model parameters

Looking at the numerical simulations we notice an over-shoot at the last tile of the domain. This relates to the no-flux boundary conditions. No-flux boundary conditions impose a model symmetry that allows to attach a mirror image of the domain on either boundary. If the boundary tile is of the strong type, then its outside neighbor tile is also a strong tile, in effect doubling the tile size. Hence at the last tile, the virus finds a doubled sized good habitat and can grow much larger than in a small good habitat. This over-shoot becomes less and less relevant as we go to smaller tile sizes. We also performed numerical simulations, where we added one more weak tile at the end of the interval, and the over-shoot disappeared (results not shown). These details of the virus load distributions are beyond what can be measured, and we are unable to confirm these distributions experimentally.

6. Conclusion

In this paper, we apply the method of homogenization to a spatially structured Fisher-KPP model for the virus-load of a virus infection of cell cultures. The method of homogenization is well known in physics and ecology, but here we apply it in a new way to microbiological data. The model explains the virus load dependence of the spatial arrangement of the cell cultures really well. When moving from fully separated, to partially mixed, to fully mixed plates, we move, mathematically, from an arithmetic mean of carrying capacities to a harmonic mean of those.

These observations have been made possible through the revolutionary technique of inkjet bioprinting as pioneered by Park et al (Park et al., 2017). Besides checker-board patterns, also other patterns can be printed and analysed, which is material for future research.

It should be noted that our model is spatially one dimensional, while the experiments are two dimensional. We argue that due to model symmetry a one-dimensional approach is sufficient. In fact, the model performs well, all results are within error tolerances, and we do not expect any further gain through a two dimensional version.

Biologically our results are surprising. The viral infection of a heterogeneous population is not simply an arithmetic sum of its constituents, but the spatial arrangement matters significantly. These observations will have relevance in related areas such as viral therapy of cancer, and viral infection patterns of tissue such as SARS-CoV-2.

Data Availability:

Data are in Appendix A

Acknowledgements:

AAB acknowledges support through United Arab Emirates University Scholarship. TH acknowledges support from the Natural Science and Engineering Research Council of Canada (NSERC) and a visiting professorship at the Korean Advanced Institute of Science and Technology (KAIST). AAB and TH thank the members of the Mathematical Biology Journal Club for their valuable comments.

Appendix A. Experimental Data

Here we present the raw-data as measured in our viral load experiments for the mixed plate and the plates with inner square of 1.5 mm, 3 mm, and 5 mm side length. Table A.5 and A.6 represent the kinetics of influenza A virus in weak and strong population in first and second experiment with triplicate data sets. While table A.7, represents the viral load for the different inner sizes in the micro-pattering at one day.

Sample name	**CT**	**mGAPDH**	**Normalization CT**	**Normalization mGAPDH**	**RQ**
Weak 0h-1	32.906	13.687	N.D	N.D	N.D
Weak 0h-2	33.670	14.912	N.D	N.D	N.D
Weak 0h-3	33.175	15.184	N.D	N.D	N.D
Strong 0h-1	33.714	14.757	N.D	N.D	N.D
Strong 0h-2	34.002	13.825	N.D	N.D	N.D
Strong 0h-3	34.402	14.588	N.D	N.D	N.D
Weak 6h-1	22.480	16.430	6.0500	0.1090	0.9272
Weak 6h-2	22.681	16.685	5.9960	0.0550	0.9626
Weak 6h-3	22.137	16.360	5.7770	-0.1640	1.1204
Strong 6h-1	21.071	15.869	5.2020	-0.7390	1.6690
Strong 6h-2	20.420	15.398	5.0220	-0.9190	1.8908
Strong 6h-3	20.254	15.299	4.9550	-0.9860	1.9807
Weak 12h-1	20.533	15.500	5.0330	-0.9080	1.8764
Weak 12h-2	20.690	15.757	4.9330	-1.0080	2.0111
Weak 12h-3	20.611	15.687	4.9240	-1.0170	2.0237
Strong 12h-1	19.745	15.780	3.9650	-1.9760	3.9340
Strong 12h-2	19.875	15.901	3.9740	-1.9670	3.9095
Strong 12h-3	19.902	15.728	4.1740	-1.7670	3.4035
Weak 24h-1	20.008	14.719	5.2890	-0.6520	1.5713
Weak 24h-2	20.184	14.417	5.7670	-0.1740	1.1282
Weak 24h-3	19.864	13.947	5.9170	-0.0240	1.0168
Strong 24h-1	17.433	13.385	4.0480	-1.8930	3.7141
Strong 24h-2	18.039	14.757	3.2820	-2.6590	6.3160
Strong 24h-3	18.447	14.939	3.5080	-2.4330	5.4002

Table A.5: The growth rate of influenza A virus in weak and strong population in first experiment with three data sets for one day. N.D means not determined

Sample name	**CT**	**mGAPDH**	**Normalization CT**	**Normalization mGAPDH**	**RQ**
Weak 0h-1	N.D	13.927	N.D	N.D	N.D
Weak 0h-2	N.D	14.059	N.D	N.D	N.D
Weak 0h-3	37.975	14.316	N.D	N.D	N.D
Strong 0h-1	N.D	14.942	N.D	N.D	N.D
Strong 0h-2	36.907	14.285	N.D	N.D	N.D
Strong 0h-3	N.D	13.836	N.D	N.D	N.D
Weak 6h-1	24.539	19.245	5.2940	-0.3600	1.2834
Weak 6h-2	23.796	17.951	5.8450	0.1910	0.8760
Weak 6h-3	23.748	17.925	5.8230	0.1690	0.8895
Strong 6h-1	21.493	16.308	5.1850	-0.4690	1.3841
Strong 6h-2	21.513	16.950	4.5630	-1.0910	2.1302
Strong 6h-3	20.211	15.401	4.8100	-0.8440	1.7950
Weak 12h-1	18.613	15.948	2.6650	-2.9890	7.9390
Weak 12h-2	19.146	16.261	2.8850	-2.7690	6.8164
Weak 12h-3	19.805	17.057	2.7480	-2.9060	7.4950
Strong 12h-1	16.076	14.713	1.3630	-4.2910	19.576
Strong 12h-2	16.607	15.885	0.7220	-4.9320	30.527
Strong 12h-3	15.965	14.355	1.6100	-4.0440	16.495
Weak 24h-1	20.678	14.778	5.9000	0.2460	0.8432
Weak 24h-2	20.581	15.002	5.5790	-0.0750	1.0534
Weak 24h-3	20.570	14.960	5.6100	-0.0440	1.0310
Strong 24h-1	15.642	14.052	1.5900	-4.0640	16.726
Strong 24h-2	16.010	13.580	2.4300	-3.2240	9.3437
Strong 24h-3	15.060	13.967	1.0930	-4.5610	23.605

Table A.6: The growth rate of influenza A virus in weak and strong population in second experiment with three data sets for one day. N.D means not determined

Size of inner square	**CT**	**CT (GAPDH)**	**RQ**	**Average**
Mix-1	15.366	15.157	1.0669	
Mix-2	14.849	15.013	1.3816	1.2957
Mix-3	14.695	14.917	1.4387	
1.5 mm-1	15.148	14.845	1.0000	
1.5 mm-2	15.172	15.395	1.4396	1.3305
1.5 mm-3	15.461	15.793	1.5520	
3 mm-1	14.621	15.638	1.7034	
3 mm-2	15.266	15.087	1.2569	1.9304
3 mm-3	14.440	15.294	2.8308	
5 mm-1	14.191	15.060	2.2519	
5 mm-2	14.948	16.609	3.8978	3.3996
5 mm-3	14.547	16.262	4.0492	

Table A.7: The influenza A viral load on the micro-patterning for the different inner square sizes with three data set at one day.

References

H. Now, J.-Y. Yoo, Ag490 and pf431396 sensitive tyrosine kinase control the population heterogeneity of basal stat1 activity in ube1l deficient cells, PloS one 11 (2016) e0159453.

B. Snijder, R. Sacher, P. Rämö, E.-M. Damm, P. Liberali, L. Pelkmans, Population context determines cell-to-cell variability in endocytosis and virus infection, Nature 461 (2009) 520–523.

J. A. Park, S. Yoon, J. Kwon, Y. K. Kim, W. J. Kim, J. Y. Yoo, S. Jung, Freeform micropatterning of living cells into cell culture medium using direct inkjet printing, Scientific reports 7 (2017) 1–11.

I. Li, K. Chan, K. To, S. Wong, P. Ho, S. Lau, P. Woo, H. Tsoi, J. Chan, V. Cheng, et al., Differential susceptibility of different cell lines to swine-origin influenza A H1N1, seasonal human influenza A H1N1, and avian influenza A H5N1 viruses, Journal of Clinical Virology 46 (2009) 325–330.

E. De Vries, D. M. Tscherne, M. J. Wienholts, V. Cobos-Jimenez, F. Scholte, A. Garcia-Sastre, P. J. Rottier, C. A. De Haan, Dissection of the influenza A virus endocytic routes reveals macropinocytosis as an alternative entry pathway, PLoS Pathog 7 (2011) e1001329.

A. Smith, A. Perelson, Influenza A virus infection kinetics: quantitative data and models, WIREs Syst. Biol. Med. 3 (2011) 429–445.

C. Beauchemin, A. Handel, A review of mathematical models of influenza A infections within a host or cell culture: lessons learned and challenges ahead, BMC Public Health 11 (2011) S7.

M. Gallagher, C. Brooke, R. Ke, K. Koelle, Causes and consequences of spatial within-host viral spread, Viruses 10 (2018) 627–650.

A. Smith, Host-pathogen kinetics during influenza infection and coinfection: insights from predictive modeling, Immunological Reviews 285 (2018) 97–112.

D. Wodarz, A. Hofacre, J. W. Lau, Z. Sun, H. Fan, N. L. Komarova, Complex spatial dynamics of oncolytic viruses in vitro: mathematical and experimental approaches, PLoS Comput Biol 8 (2012) e1002547.

V. L. de Rioja, N. Isern, J. Fort, A mathematical approach to virus therapy of glioblastomas, Biology Direct 11 (2016) 1.

J. D. Murray, Mathematical Biology: II. Spatial Models and Biomedical Applications, Springer Science & Business Media, 3 edition, 2007.

N. Shigesada, K. Kawasaki, E. Teramoto, Traveling periodic waves in heterogeneous environments, Theoretical Population Biology 30 (1986) 143–160.

N. Shigesada, K. Kawasaki, H. F. Weinberger, Spreading speeds of invasive species in a periodic patchy environment: Effects of dispersal based on local information and gradient-based taxis, Japan Journal of Industrial and Applied Mathematics 32 (2015) 675–705.

G. A. Maciel, F. Lutscher, How individual movement response to habitat edges affects population persistence and spatial spread, The American Naturalist 182 (2013) 42–52.

R. A. Fisher, The wave of advance of advantageous genes, Annals of Eugenics 7 (1937) 355–369.

A. N. Kolmogorov, I. G. Petrovskii, N. S. Piskunov, A study of the diffusion equation with increase in the amount of substance, and its application to a biological problem, Bull. Moscow Univ., Math. Mech. 1:6 (1937) 1–26.

G. A. Pavliotis, A. M. Stuart, Multiscale Methods: Averaging And Homogenization, Springer Science & Business Media, 2008.

M. H. Holmes, Introduction To Perturbation Methods, Springer Science & Business Media, 2 edition, 2012.

M. J. Garlick, J. A. Powell, M. B. Hooten, L. R. McFarlane, Homogenization of large-scale movement models in ecology, Bulletin of Mathematical Biology 73 (2011) 2088–2108.

G. A. Maciel, F. Lutscher, Allee effects and population spread in patchy landscapes, Journal of Biological Dynamics 9 (2015) 109–123.

B. P. Yurk, Homogenization analysis of invasion dynamics in heterogeneous landscapes with differential bias and motility, Journal of Mathematical Biology 77 (2018) 27–54.

B. P. Yurk, C. A. Cobbold, Homogenization techniques for population dynamics in strongly heterogeneous landscapes, Journal of Biological Dynamics 12 (2018) 171–193.

A. G. Murray, G. A. Jackson, Viral dynamics: a model of the effects of size, shape, motion and abundance of single-celled planktonic organisms and other particles, Marine Ecology Progress Series 89 (1992) 103–116.

R. G. Bacabac, T. H. Smit, S. C. Cowin, J. J. Van Loon, F. T. Nieuwstadt, R. Heethaar, J. Klein-Nulend, Dynamic shear stress in parallel-plate flow chambers, Journal of Biomechanics 38 (2005) 159–167.

G. D. Smith, Numerical Solution Of Partial Differential Equations: Finite Difference Methods, Oxford University Press, 3 edition, 1985.